

## Electronic supplementary information (ESI) for

### Atomically resolved interfacial water structures on crystalline hydrophilic and hydrophobic surfaces

Manuel Ralph Uhlig<sup>1</sup>, Simone Benaglia<sup>1</sup>, Ravindra Thakkar<sup>2</sup>, Jeffrey Comer<sup>2</sup>, Ricardo Garcia<sup>1,\*</sup>

<sup>1</sup>*Instituto de Ciencia de Materiales de Madrid, CSIC, c/ Sor Juana Ines de la Cruz 3, 28049 Madrid, Spain*

<sup>2</sup>*Nanotechnology Innovation Center of Kansas State, Department of Anatomy and Physiology, Kansas State University, Manhattan, Kansas, 66506, USA*

\*Corresponding author. Ricardo Garcia. E-mail: [r.garcia@csic.es](mailto:r.garcia@csic.es)

#### **This PDF file includes:**

Supplementary text  
Figures S1 to S13  
Tables S1 to S2  
ESI References

## Supplementary Information Text

### 3D-AFM

The experiments were performed with a home-made 3D-AFM (1, 2). The oscillation of the cantilever was driven by photothermal excitation. The free amplitude values  $A_0$  were in the range of 70–90 pm. Fig. S1 shows the dependence of the amplitude and the phase on the tip–sample distance for the different solid–liquid interfaces. The feedback monitors the instantaneous amplitude and acts on the z-piezo to keep the lowest amplitude reached during the approach close to a fixed value ( $A_{sp} \approx 0.75\text{--}0.50 A_0$ ). We have used a relatively low feedback bandwidth (2 kHz). The feedback response is too slow to compensate for the applied z-piezo displacement signal but fast enough to track the topography of the surface and correct for sample tilt, piezo creep, and remaining thermal drift.

### High-resolution AFM imaging

AFM images on the HOPG and the h-BN surfaces in liquid were obtained in the amplitude modulation (AM) mode by exciting either the first or the second mode of the cantilever. The free amplitudes  $A_0$  were typically of 200–500 pm. The images taken over the ripple structures have been performed using ArrowUHF AuD, ArrowUHF Al, PPP-NCHAuD, PPP-FMAuD (all NanoAndMore, Germany) and FastScan-A (Bruker, USA) cantilevers excited in the first or in the second mode. The set-point amplitude was set as  $A_{sp} = 0.70\text{--}0.80 A_0$ .

The ripple structures were imaged after some hours of incubation over a newly exfoliated surface. Air-aged samples already presented these arrangements, suggesting that the ripples are connected to molecules existing in the air. After immersion into liquid, additional molecules can adsorb to the surface; these molecules are present already as contaminants in the ultrapure water itself or are incorporated into the water by reaching equilibrium with the air. An example of ripple structures over a HOPG surface is shown in Fig. S2. It's worth pointing out the presence of structures with different orientations, ruling out common imaging artifacts as the source of the ripples. The small amplitude used here allows us to achieve the resolution needed to observe the ripples (3) and the  $\approx 0.5$  nm periodic structure associated with the molecular stacking of hydrocarbon backbones within the ripples (Fig. 5b, main text). For larger values of  $A_0$  the ripple structure cannot be resolved. This is illustrated in Fig. S3: when  $A_0$  becomes higher than 1.5 nm the ripples are not visible anymore.

The high resolution images of the lattice of the HOPG and h-BN (Fig. 5b-c, main text) were obtained using PPP-NCHAuD cantilevers (NanoAndMore, Germany) excited in the second mode. Lattice contrast was achieved by reducing the set-point amplitude to  $A_{sp} = 0.30\text{--}0.50 A_0$ .

### Calibration of the microcantilevers

The cantilevers were calibrated using the GetReal® feature of the Asylum Research Software(4–6). GetReal® provides a contactless calibration method and hence can be performed before the experiment without risking to damage the tip. In short, it works as described in the following. The superscripts “air” and “lq” denote quantities that correspond specifically to air and liquid, respectively.

First, the cantilever's thermal noise spectrum (power spectral density, PSD) is recorded in air.

Then, the first mode's q-factor and resonance frequency in air,  $Q_1^{\text{air}}$  and  $f_1^{\text{air}}$ , are determined from the PSD spectrum. Following the so-called  $Qf^{1.3}$  scaling method (4, 5)  $k_1$  can be obtained from  $Q_1^{\text{air}}$  and  $f_1^{\text{air}}$  through

$$k_1 = k_{\text{ref}} \left( \frac{Q_1^{\text{air}}}{Q_{\text{ref}}} \right) \left( \frac{f_1^{\text{air}}}{f_{\text{ref}}} \right)^{1.3}$$

(ES1) with  $k_{\text{ref}}$ ,  $Q_{\text{ref}}$ , and  $f_{\text{ref}}$  being the reference values for the first mode's stiffness, Q-factor, and resonance frequency, respectively. These reference values were measured *in factory* on a set of cantilevers of the same type using a laser Doppler vibrometer (in air). Once this step was completed, the cantilever was immersed in the liquid, and its PSD spectrum was recorded again. Using the calculated  $k_1$ , the single harmonic oscillator (SHO) model is fitted to the PSD spectrum around the peak of the first mode's resonance frequency in liquid,  $f_1^{\text{liq}}$  (7). From the fit, the corresponding inverse optical lever sensitivity (invOLS) in liquid,  $\sigma_1^{\text{liq}}$ , is obtained.

For some measurements, the second mode was also calibrated in liquid (in the case of using PPP-NCHAuD). The resonance frequency of the second mode,  $f_2^{\text{liq}}$ , is measured from the PSD and the corresponding force constant,

$$k_2 = k_1 \left( \frac{f_2^{\text{liq}}}{f_1^{\text{liq}}} \right)^{2.17}$$

(ES2) is calculated as proposed by Labuda *et al.* (6). Knowing  $k_2$ , the SHO model is then fitted to the PSD around the peak of the second resonance frequency to obtain the corresponding invOLS  $\sigma_2^{\text{liq}}$  and  $Q_2^{\text{liq}}$ .

The obtained values are summarized in Table S1.

### Reconstruction of the tip-sample force from the observables

The 3D-AFM (8) was operated in the AM mode (9). This mode provides as the main observables the oscillation amplitude  $A$  and the phase shift  $\phi$ . Force-distance curves (force curves) were computed from these observables as a function of the z-position (10–12) Here, we have used Hölischer's algorithm (12) implemented into a custom written code (Igor Pro, Wavemetrics, USA). The procedure is illustrated for an average force curve in Fig. S4. First, the raw data is averaged over 80 individual curves (Fig. S4). Then, we follow the steps described in ref (12). Before calculating the derivative, we apply a slight binomial smoothing (range of 2) to avoid spikes due to noise in the raw data. The obtained force curve is shown in Fig. S4c (in black).

The z-range of the force-distance curves was slightly reduced with respect to the amplitude and phase shift-distance curves (reduced by the zero-to-peak amplitude, *i.e.*,  $A_0$ ) because the force reconstruction process required an integration over the oscillation cycle.

### Considerations on the ripple structures

Ripple structures were found and studied in air and in liquid with different techniques over several layered materials, such as graphitic surfaces, h-BN and WSe<sub>2</sub> (2, 13–18). The origin of these structures was attributed to contaminants present in the air which assemble over the surface of the layered material. The high-resolution structures of about 0.5 nm periodicity (Fig. 4b of the main text) was previously shown, but not attributed to any specific molecular structure (18, 19). Interestingly, as aforementioned, their presence was studied not only by atomic force microscopy but also more recently through optical measurements, such as polarization-contrast microscopy (16), which ruled out the possibility of structural rippling. Finally, the formation of an adlayer in liquid environment was reported through the use of electrochemical impedance spectroscopy and

scanning electrochemical microscopy and attributed to the accumulation of contaminants on the material's surface (20–22). These techniques do not have the high-spatial resolution capabilities of AFM to resolve the ripple structures with molecular detail. However, they provide a possibility to record the effect of the formation of the adlayer on the electrochemical properties of the underlying material.

### Experiments in *n*-pentadecane (C<sub>15</sub>H<sub>32</sub>)

3D-AFM experiments were performed by immersing HOPG in *n*-pentadecane. Figure S5a shows a representative 2D-AFM *xz* force map of the HOPG-C<sub>15</sub>H<sub>32</sub> interface. The interlayer spacing (Fig. S5b) is  $0.47 \pm 0.03$  nm. This value indicates that the linear hydrocarbon chains are oriented in parallel to the HOPG surface. No ordering of the liquid was detected for tip-sample distances of  $\geq 2.0$  nm.

### Experiments on HOPG (fresh) surfaces

3D-AFM experiments were performed on cleaved HOPG surfaces that were immediately immersed in ultrapure water after cleavage (<2 s). In many experiments, we observed interlayer spacings below 0.4 nm (Fig. S6a). The interlayer spacings (Fig. S6b) were  $d_1=0.26$  nm and  $d_2=0.37$  nm. No ordering of the liquid was detected for tip-sample distances of  $\geq 1.5$  nm.

### Molecular dynamics protocols

The molecular dynamics simulations followed protocols validated against experiment in our previous work (23, 24). All simulations were performed with NAMD 2.13 (25). Lennard-Jones interactions were calculated with a smooth 1.0–1.2 nm cutoff. For all simulations except the energy dissipation calculations, the pressure was maintained at 1.01325 bar using the Langevin piston method (26) and the temperature was maintained at 295 K using a Langevin thermostat with a damping parameter of  $1 \text{ ps}^{-1}$ . All simulations were performed with mass repartitioning (27) of non-water hydrogen atoms (with the mass increased by a factor of 3). The equations of motion were integrated with a 3 fs time step. Electrostatic interactions were calculated using the particle-mesh Ewald method (28) with a grid spacing < 0.12 nm. Water molecules were represented by the TIP3P model (29) of the CHARMM force field and kept rigid using the SETTLE (30) method. The lengths of other covalent bonds involving hydrogen were constrained (31). For organic molecules and graphitic carbon, interatomic interactions were represented using the CHARMM General Force Field (CGenFF) (32), version 4.3. We have previously demonstrated that this force field agrees well with experiment for the thermodynamics of adsorption of small organic molecules on graphitic carbon in aqueous solution (23, 24) as well as in organic solvents (33). Muscovite mica was represented using CLAYFF (34, 35). Previous studies (36–39) have validated the combination of CLAYFF with the CHARMM force field framework (40). Of the solvent compounds considered, only 3-methylpentane, 2-ethylhexanol, and limonene lacked standard parameterizations in CGenFF. These compounds were parameterized using the CGenFF web interface (41, 42).

### Molecular dynamics systems

The graphite systems included two rectangular graphene sheets stacked atop one another and aligned perpendicular to the *z*-axis, with mean dimensions of  $2.935 \times 2.966 \text{ nm}^2$ . As in previous work (23, 24, 43), the atoms of the lower sheet were harmonically restrained to their initial *z* position. All calculations of surface interactions were performed relative to the upper sheet, to which no restraints were applied. The muscovite mica surface was created by a  $2 \times 2$  replication of the final structure given by Wang et al. (35) to produce a two layer mica sheet with mean dimensions of  $3.583 \times 4.140 \text{ nm}^2$ . Tetrahedral aluminum atoms in the bottom layer were harmonically restrained to their initial *z* positions. Again, all calculations of surface interactions were performed relative to the unrestrained upper layer of mica. Water molecules were added

using VMD (44) to create mica–water and graphite–water systems with mean  $z$  dimensions of 5.19 and 5.66 nm, respectively. Simulation systems including organic solvents were constructed using the program PackMol (43) to yield systems with  $z$  dimensions of 5.37 nm. All systems underwent 2000 steps of energy minimization and 150 ps of equilibration before beginning production simulations.

### Tip model construction

Tip asperity models were assembled using the program Avogadro (45) and custom scripts employing the TopoTools module (46) of the program VMD (44). The experiments made use of silicon tips, treated to obtain a hydrophilic surface. Some CHARMM-compatible silicon dioxide models (47) were created; however, because that carbon-based structures are better supported by the force field, we settled on hydroxylated diamondoid structures. The magnitudes of the forces measured in the experiment were quite small and could only be obtained when the contact area between the tip asperity model and surface was a few atoms. All tip asperity models that were relatively hydrophilic (including a high density of surface alcohol or silanol groups) produced qualitatively similar force profiles. The final tip asperity model (shown in Fig. 3(a)-(c)) was built from a diamondoid carbon framework with threefold symmetry about the  $z$  axis. A methyl group was added to the central carbon protruding on the surface-facing end of the diamondoid. This group would be the only portion of the model to make direct contact with the mica or graphite surfaces. The remaining 27 carbon atoms having one dangling bond were capped with OH groups, whereas the remaining 24 having two dangling bonds were capped with two hydrogen atoms. The complete model had an empirical formula  $C_{89}H_{80}O_{27}$ . The tip asperity model was parameterized with CGenFF the ParamChem web interface (41, 42).

### Force-distance curve calculation

The force profiles shown in Fig. 3d,e,f (main text) were efficiently computed using the adaptive biasing force (ABF) method (48, 49) as implemented in the Colvars module (50) of NAMD. The ABF method gives direct access to the mean force on the tip asperity model as a function of distance from the surface, while also enhancing sampling of different distances. Specifically, the transition coordinate,  $Z$ , to which ABF was applied was defined as the difference in the  $z$  coordinates of the center of mass of the tip asperity model and the center of mass of the surface atoms. For mica systems, these surface atoms were the upper layer of tetrahedral aluminum atoms, whereas they were the upper graphene sheet for graphite systems. The domain of the transition coordinate was  $1.08 \leq Z \leq 2.50$  nm for mica systems and  $1.05 \leq Z \leq 2.50$  nm for graphite systems. The grid spacing was 5 pm. To emulate an AFM tip attached to a relatively rigid cantilever, the root-mean-square deviation (RMSD) of the atoms of the tip asperity model from their initial positions was restrained using the “rmsd” collective variable and Colvars options “rotateReference off” and “centerReference on”, which permitted translation of the tip asperity model while keeping its orientation fixed. For each molecular system, we performed three independent ABF calculations, with each of the three representing more than 1  $\mu$ s of simulated time. Convergence of the forces was verified by comparing the force profiles between these three calculations. The plots in Fig. 3d-f are sampling-weighted averages of the three resulting force profiles, representing a total simulated time  $>3.5$   $\mu$ s for each system.

While the precise coordinates of the surface atoms in the simulations are known, the same cannot be said for the experiments. Hence, to compare force profiles derived from simulation to those derived from experiment, it was necessary to align the force profiles from simulation. For Fig. 3d and Fig. 3f, we shifted the force profile from the simulations horizontally until the global minimum force of the calculated curve coincided with the global minimum force of the corresponding experimental curve. Aligning the graphite+ $H_2O$  curve in Fig. 3e was more difficult, due to its large deviation from the experimental curve. Given that extrema of the experimental force profile for HOPG+ $H_2O$  coincide with those of HOPG+hexane, we shifted the graphite+ $H_2O$  curve in Fig. 3e by the same distance that we shifted the graphite+hexane curve in Fig. 3f.

Hence, the horizontal axes for HOPG+H<sub>2</sub>O (Fig. 3e) and HOPG+hexane (Fig. 3f) force profiles represent equal distances from the top graphite layer.

### **Correlation between interlayer spacing and the chemical structure of the solvent**

Figure S7 shows the mass density of different solvent molecules (linear and aromatic hydrocarbons) as function of distance  $z$  from muscovite mica or graphite surfaces calculated from molecular dynamics simulations. These profiles reveal the link between the structure of the solvation layers and the chemical structure of the solvent.

### **Adsorption free energy calculations**

The adsorption free energies shown in Fig. S8 were computed with ABF using a definition of the transition coordinate similar to that employed for the force profile calculations, where organic solutes replaced the tip asperity model. In contrast to the restraint used for the tip asperity model, no RMSD restraint was applied to the solutes, since they represented free molecules. Each free energy calculation comprised  $>0.5 \mu\text{s}$  of simulated time.

### **Diffusivity calculation**

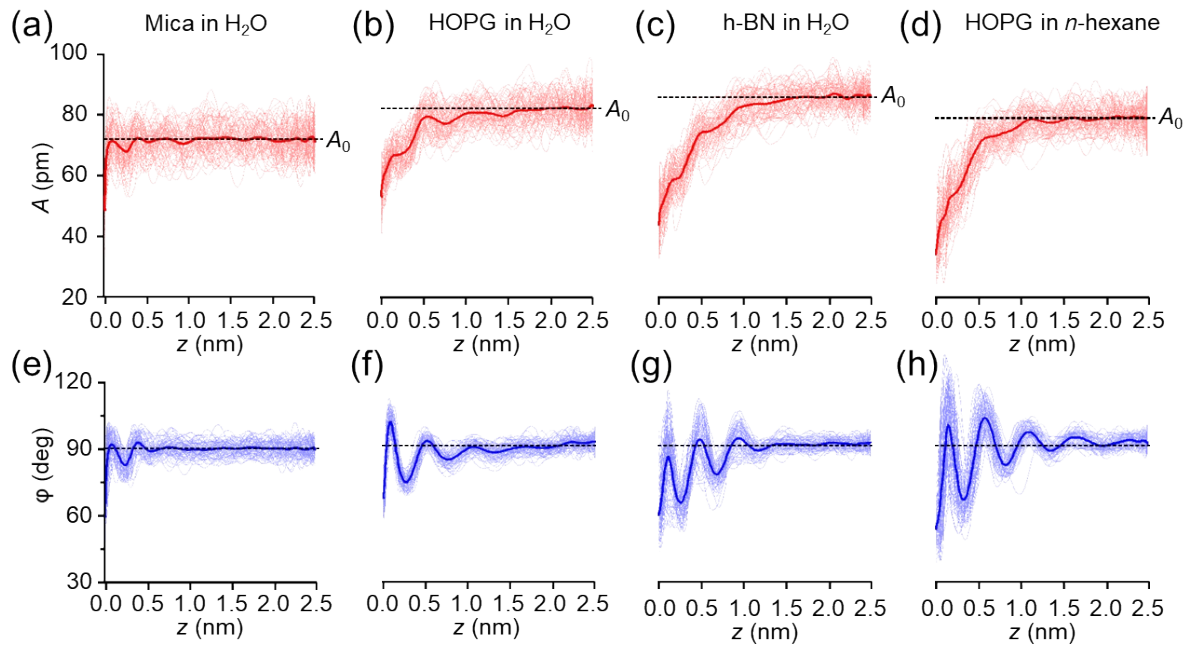
The diffusivity of hexane molecules in hexane as a function of distance from the graphene surface were calculated from an unbiased graphite–hexane simulation using the program DiffusionFusion (51). This program implements a Bayesian inference scheme (52) to estimate the diffusivity from the MD trajectories on nonuniform free-energy surfaces (53). The calculation includes a scale invariance prior on the diffusivity as well as a smoothness prior with a characteristic slope of 5 nm/ns (54). The result of this calculation is shown in Fig. S9.

### **Zero of the $z$ -coordinate**

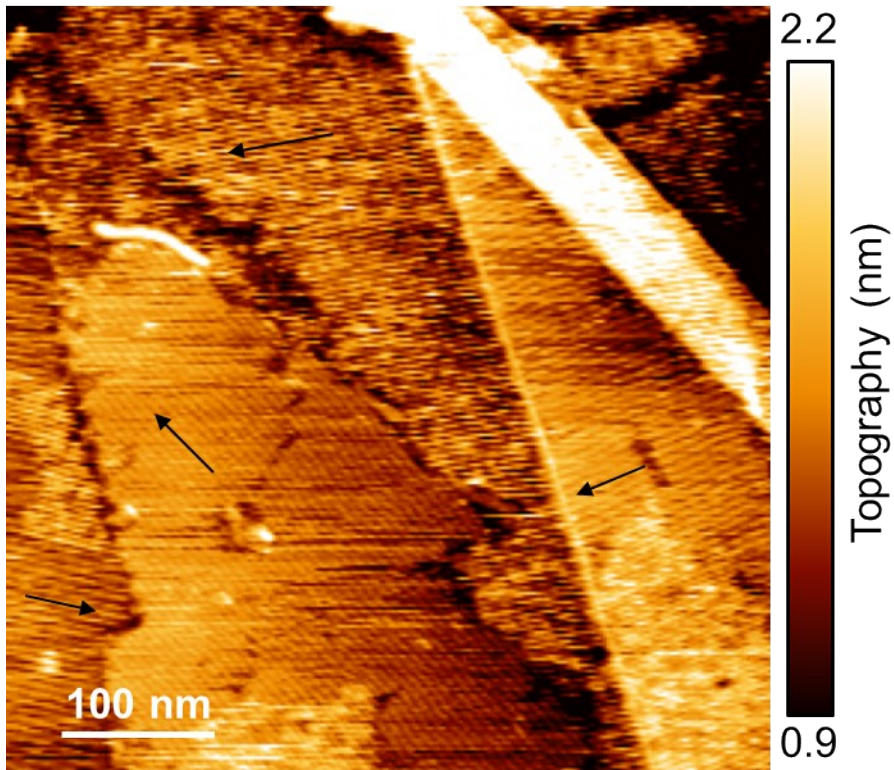
In the experiments, the position of the atoms of the surface is not known independently from the force profile; thus, the zero position is arbitrary and does not necessarily represent the point of physical contact. In fact, our simulations suggest it does not. As shown in Fig. S10, the equilibrium position (position of zero mean force and minimum free energy) for the graphite–water system corresponds to near physical contact between the tip and graphite (with physical contact defined by the van der Waals surfaces of the atoms). Surprisingly, however, for the graphite–hexane system, this same position is associated with a strong repulsive force (190 pN) on the tip asperity. The hexane solvation layer is thicker than that of water; hence, this close contact between the tip and graphite requires desolvation of a larger area of the surface, which is thermodynamically unfavorable. Consequently, the equilibrium position for graphite–hexane system lies at a separation 0.12 nm larger, where the tip asperity does not make direct contact with the graphite, but displacement of hexane from the interface is more modest. Hence, actual contact between the tip and graphite appears to occur at negative values of the coordinate used for the experimental force profiles.

Figure S11 shows the complete force profile for the graphite–water simulation. Because the characteristic length of the force oscillations is shorter than in experimental profile, no choice of shifting the  $z$ -axis gives even qualitative agreement with experiment. On the other hand, the result of the graphite–hexane simulation agrees relatively well with the experimental force profile in both form and magnitude, suggesting that the graphite–hexane simulation is a better model of the real "graphite–water" experiment than the model pure graphite–water model. The thermodynamics of the solvation layers near the interface between the tip and solid surface can therefore have a strong effect on the force profile. The exact magnitude of the repulsive force is

likely to depend on the curvature and physicochemistry of the tip asperity as well. The influence of the geometry and chemical structure of the tip asperity will be addressed in future work.



**Figure S1.** 3D-AFM observables. Amplitude ( $A$ ) and phase shift ( $\phi$ ) versus distance curves obtained in the 3D-AFM experiments. Amplitude-distance curves recorded on (a) mica in ultrapure water, (b) HOPG in ultrapure water, (c) h-BN in ultrapure water, and (d) HOPG in  $n$ -hexane. Phase shift-distance curves recorded on (e) mica in ultrapure water, (f) HOPG in ultrapure water, (g) h-BN in ultrapure water, and (h) HOPG in  $n$ -hexane. Each panel shows 80 individual curves. The average curves are highlighted. Amplitude and phase shift-distance curves are acquired simultaneously.



**Figure S2.** Ripples on HOPG. Ripple structures imaged in ultrapure water on an air-aged HOPG. Black arrows are used to underline the different orientations of the ripples. Arrows are parallel to the ripple structures.

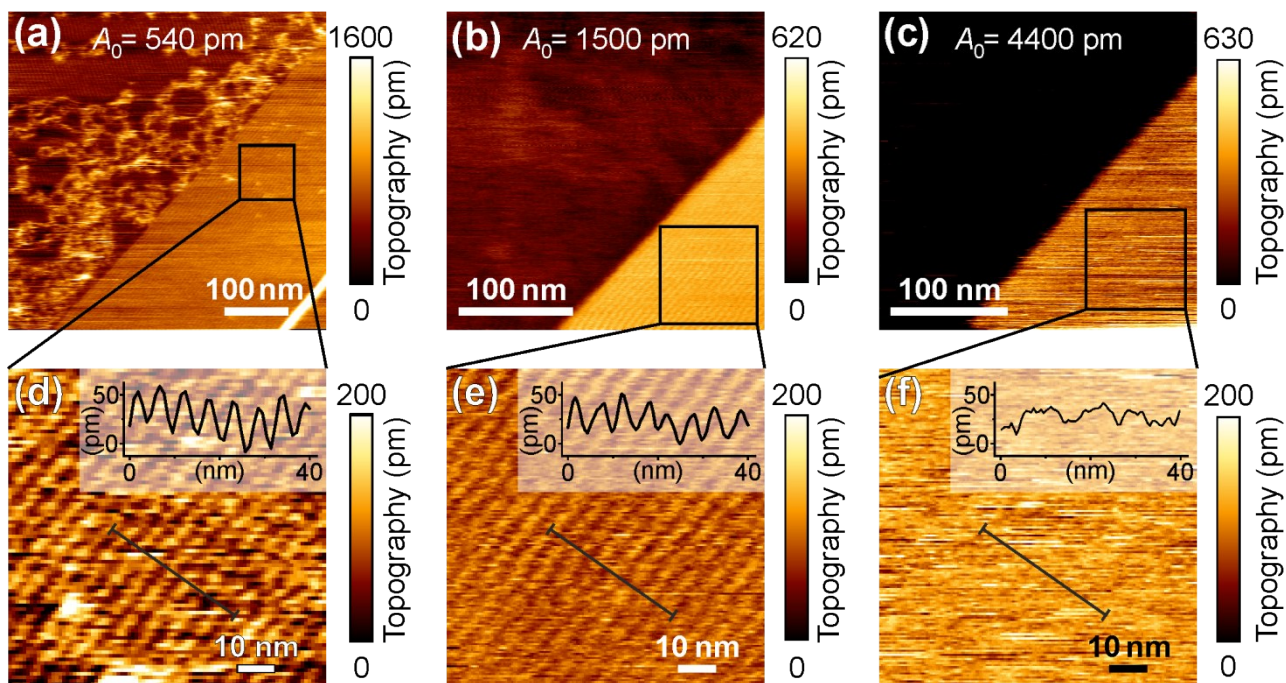


**Figure S3.** Influence of imaging parameters on the visualization of the ripples. Ripple structures on a graphitic surface immersed in ultrapure water measured with different  $A_0$ . (a), (d) at small  $A_0$  ( $< 1$  nm) the ripple structures are resolved. (b), (e) At intermediate amplitudes (1.5 nm) it is still possible to faintly see the ripples. (c), (f) At larger amplitudes ( $>4$  nm) they are not visible anymore. The insets show the cross-sections along the lines marked in panels (d), (e) and (f).

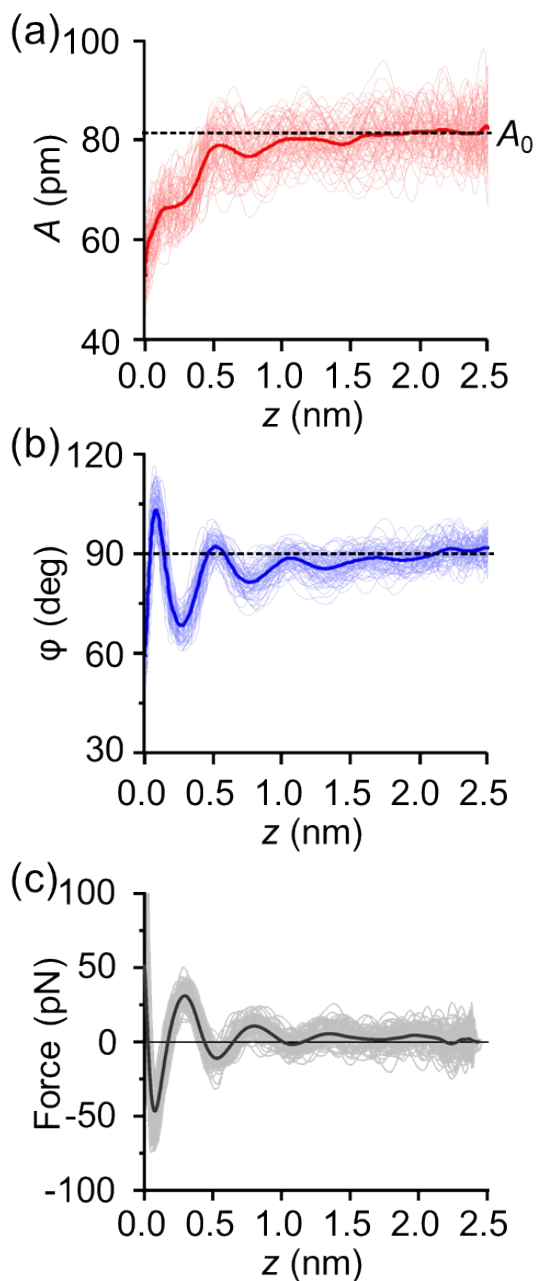


**Figure S4.** Force reconstruction taken on an HOPG surface in water. (a) Amplitude-distance curves. (b) Phase shift-distance curves. (c) Force-distance curves after processing the data from panels A and B. Each panel shows 80 individual curves. The average curve is highlighted in each panel. The  $z$ -range of the force curve is reduced with respect to the amplitude and phase shift curves by the zero-to-peak amplitude, *i.e.*,  $A_0$ . This is because the force reconstruction process requires an integration over the oscillation cycle. The parameters used to reconstruct the force are  $k_1 = 7.45$  N/m,  $Q_1 = 4.8$ ,  $f_1 = 463$  kHz,  $A_0 = 82$  pm.

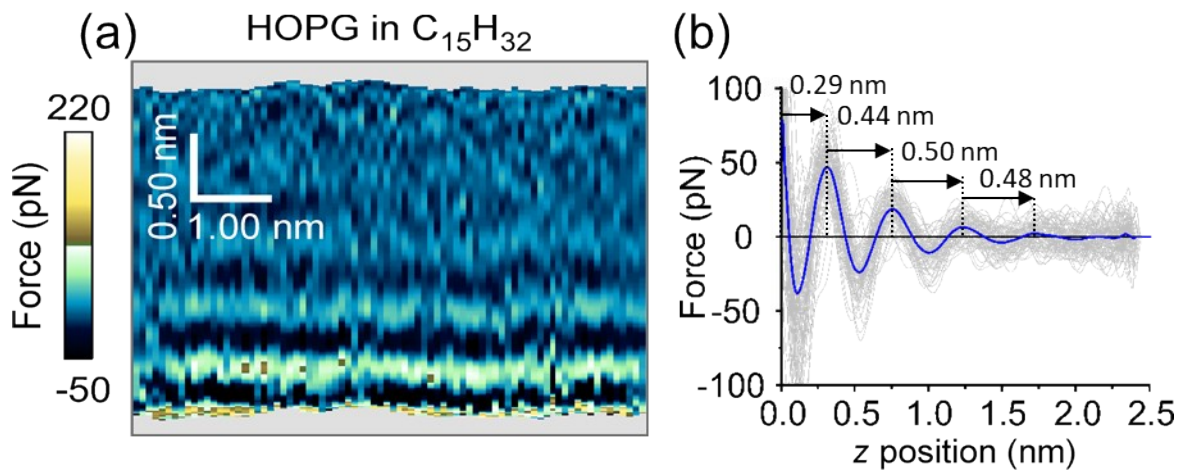


**Figure S5.** *n*-pentadecane on HOPG. (a) Two-dimensional (2D)-AFM *xz* force map of the HOPG-C<sub>15</sub>H<sub>32</sub> interface. (b) Force–distance curves (FDC) corresponding to panel (a). The averaged curve is highlighted in blue.

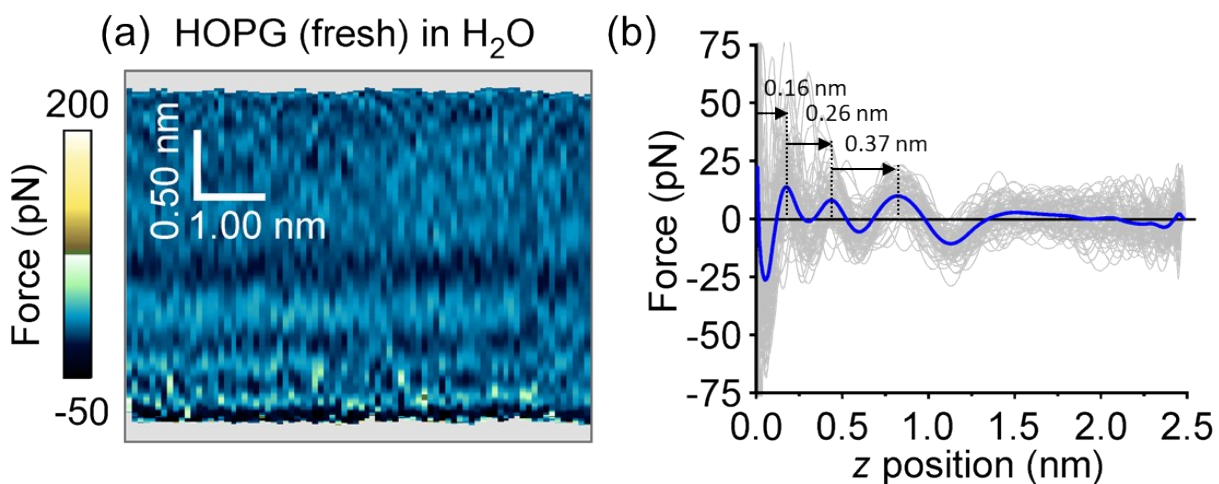


**Figure S6.** Solid-liquid interface of freshly cleaved HOPG. (a) Two-dimensional (2D)-AFM xz force map of the HOPG (fresh)-H<sub>2</sub>O interface. (b) Force–distance curves (FDC) corresponding to panel a. The averaged curve is highlighted in blue.

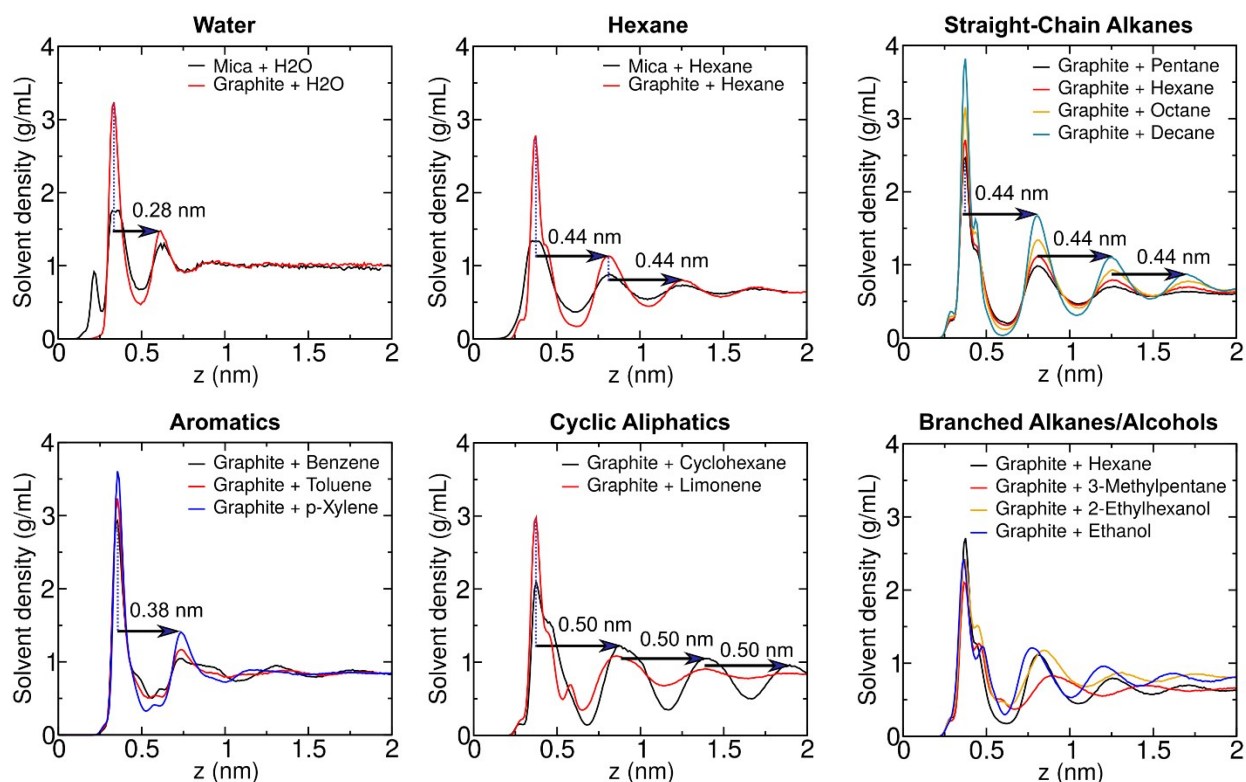


**Figure S7.** MD simulations of different liquids on mica and HOPG. Mass density of solvent molecules as function of distance ( $z$ ) from muscovite mica or graphite surfaces calculated from molecular dynamics simulations. These profiles reveal the link between the structure of the solvation layers and the chemical structure of the solvent. Water. On graphite, water shows two characteristic density peaks at distances of 0.34 and 0.62 from the plane of centers of the atoms in the first layer of graphene. This gives a peak-to-peak distance of 0.28 nm. Similar peaks are visible for mica, which also shows a peak for smaller values of  $z$  corresponding to water in unoccupied potassium ion sites. Hexane. For *n*-hexane, the density peaks appear farther from surface, at 0.38 and 0.82 nm on both graphite and water. Straight-Chain Alkanes. Like hexane, other straight chain alkanes show a first density peak at 0.38 nm and a characteristic peak spacing of 0.44 nm. Aromatics. Being flatter than alkanes, benzene and simple benzene derivatives are able to approach the surface more closely (first peak at 0.36 nm) and have a characteristic second peak at 0.74 nm. Cyclic Aliphatics. Cyclic hydrocarbons cyclohexane and limonene have a first density peak at the same location as the straight-chain alkanes (0.38 nm), but their steric bulk leads to a larger spacing between density peaks, 0.50 nm. Branched Alkanes/Alcohols. Branched alkanes and alcohols have first peaks near that of the straight-chain alkanes, but variable peak spacing. The spacing of straight-chain alkanes is most consistent with the characteristic distances observed in the experiments.

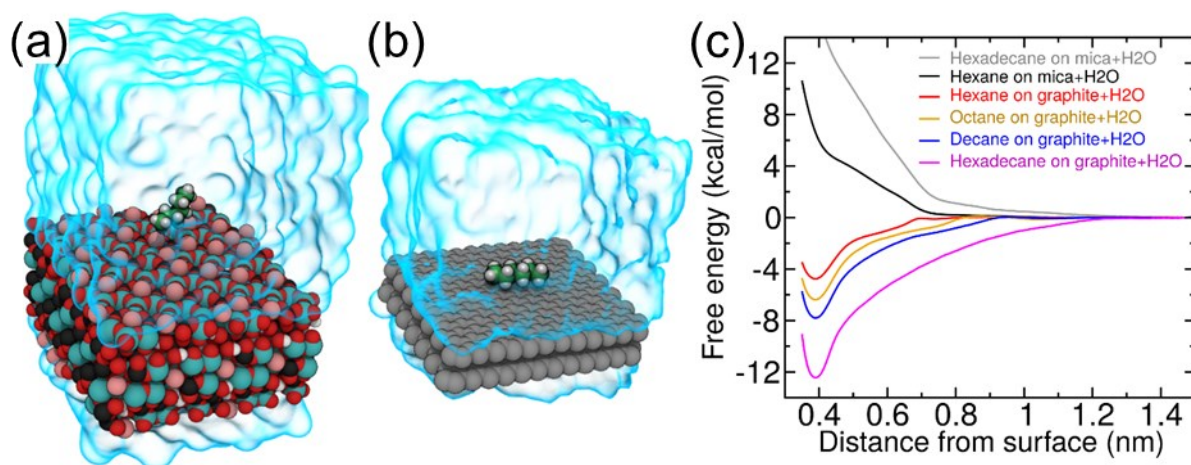


**Figure S8.** MD simulation of alkanes aqueous solution on mica and graphite. Free-energy calculations for adsorption of alkanes onto muscovite mica or graphite surfaces from aqueous solution. (a) Atomic model of an interface between muscovite mica and water including a single hexane molecule. (b) Atomic model of hexane adsorbed to a graphite–water interface. For clarity, explicit water molecules are shown as a translucent blue surface. Atoms are shown as spheres (H, white; graphite C, gray; hexane C, green; oxygen, red; K<sup>+</sup>, pink; Al, black; Si, cyan). (c) Free energy as a function of the distance between the center of mass of the alkane molecule and surface plane. Straight-chain alkanes adsorb to the graphite basal plane with an affinity that increases with the mass of the alkane. On the contrary, alkanes exhibit no affinity for muscovite mica.

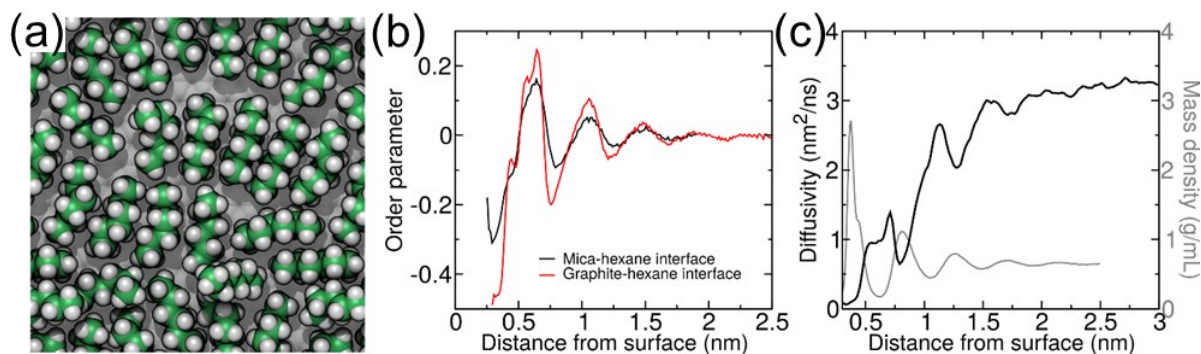


**Figure S9.** Structure of solvation layers of hexane. (a) Snapshot from an MD simulation of the first hexane layer on the graphite basal plane. Most of the hexane molecules lie parallel to the surface and some alignment of neighboring molecules is evident. (b) Orientational order parameter for hexane C–C bonds as a function of the distance from mica and graphite surfaces. The parameter is defined as the average over  $(3 \cos^2(\theta) - 1)/2$ , where  $\theta$  is the angle between the C–C bond vector and a vector perpendicular to the surface. Positive and negative values indicate a tendency for alignment perpendicular and parallel to the surface, respectively. Regions of high hexane density are associated with more alignment parallel to the surface. (c) Self-diffusion coefficient of hexane molecules as a function of distance from a graphite surface. The mass density curve is included, which makes it apparent that low diffusivity is associated with regions of high hexane density. Diffusion is particularly slow in the first solvation layer.

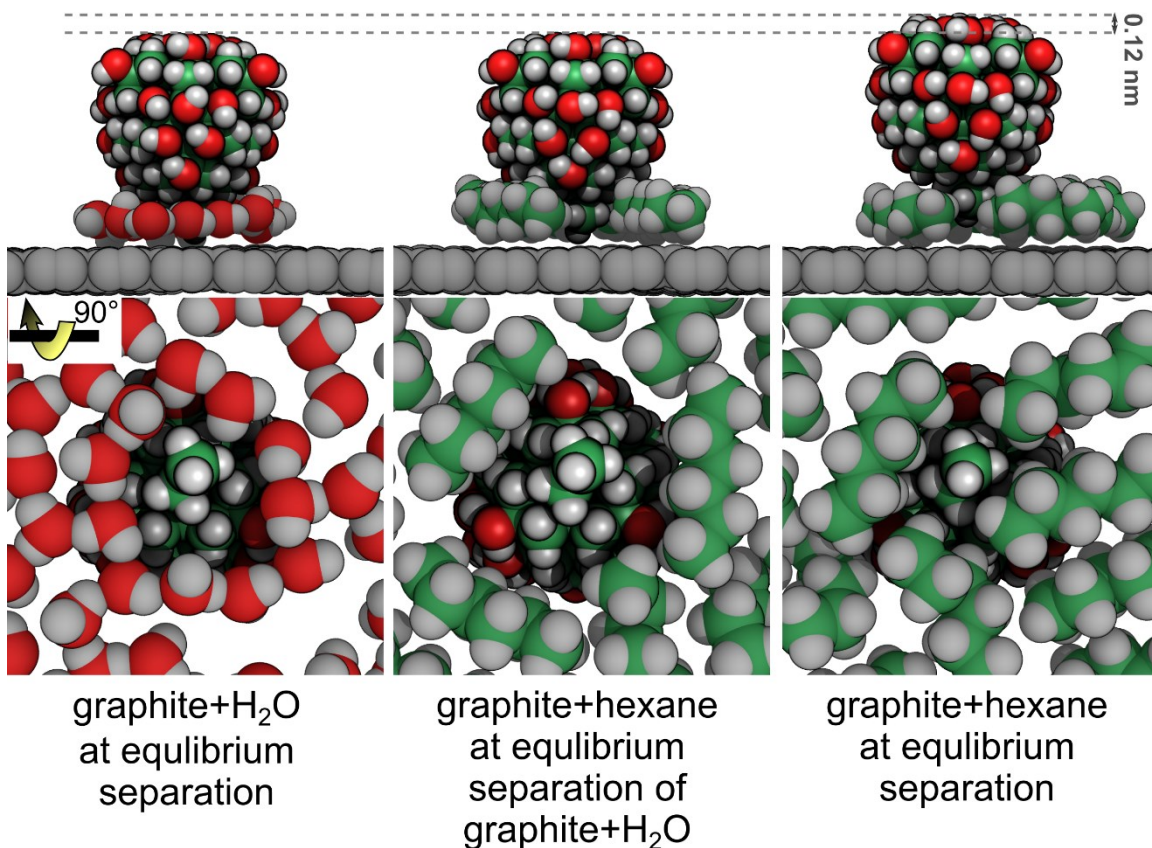


**Figure S10.** Equilibrium positions (position of zero mean force and minimum free energy) for the graphite–water (left) and graphite–hexane (right) systems. For the graphite–hexane system, the same tip’s position is associated with a strong repulsive force (190 pN) (middle panel). The hexane solvation layer is thicker than that of water; hence, this close contact between the tip and graphite requires desolvation of a larger area of the surface, which is thermodynamically unfavorable. The equilibrium position for graphite–hexane system lies at a separation 0.12 nm larger, where the tip asperity does not make direct contact with the graphite (right panel). The bottom panels show a view from the graphite surface.

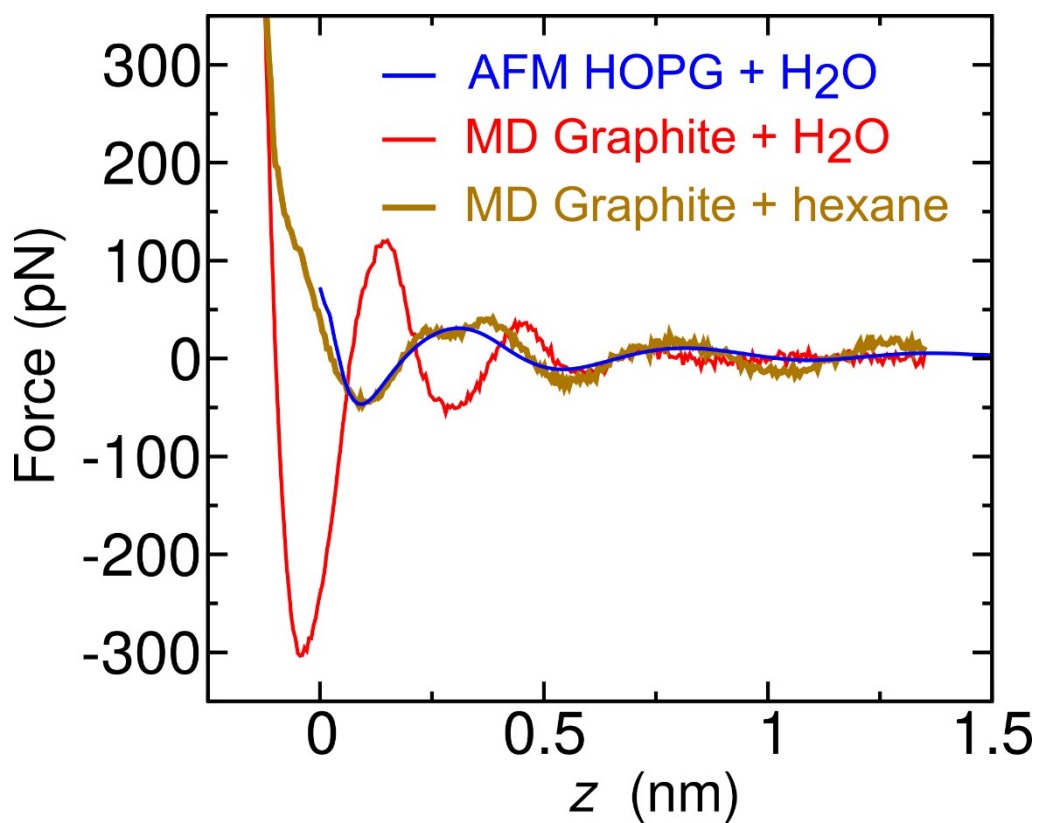


**Figure S11.** Force distance curves for different graphite-liquid interfaces. AFM stands for experiment and MD for simulations. The z-origin was chosen as the position of zero mean force and minimum free energy for the graphite-hexane interface. For that reason, there are negative distances for the simulations for graphite-water (see Fig. S10).

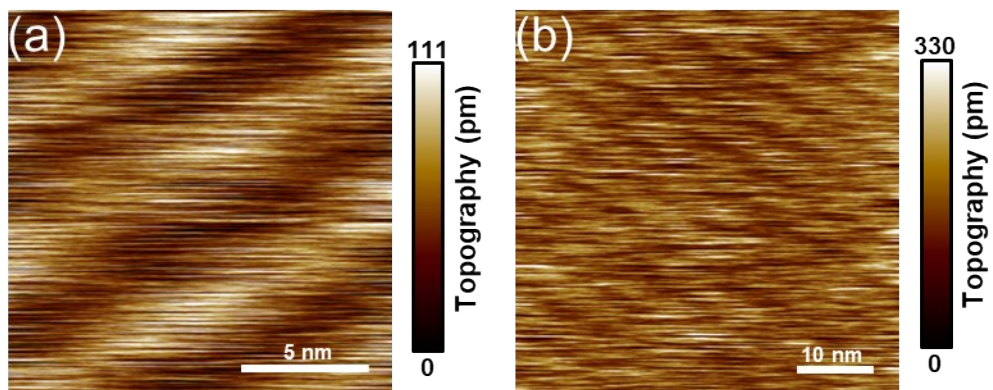


**Figure S12.** Ripple structures on HOPG (a) and hBN (b). Topographic images, respectively, of the middle panels b and c (Fig. 5, main text).

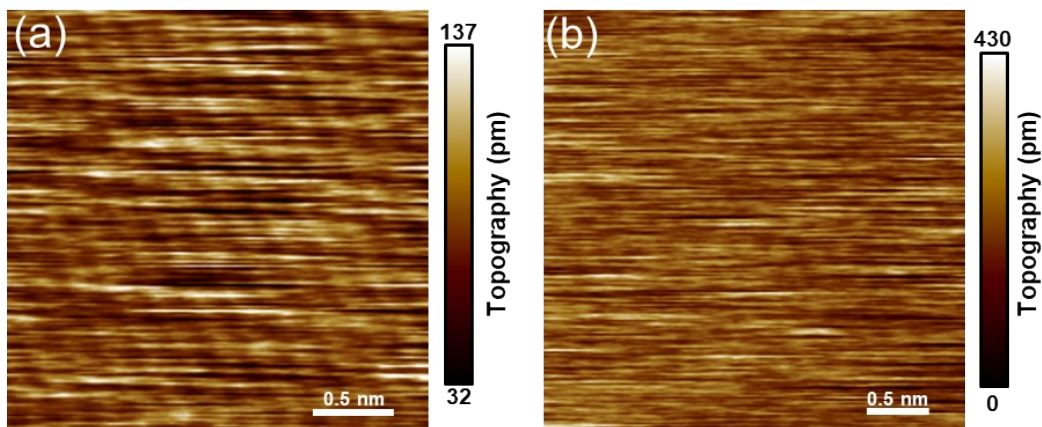


**Figure S13.** High-spatial resolution AFM image of the crystal lattice of HOPG (a) and hBN (b). Topographic images, respectively, of the regions shown in the bottom panels b and c (Fig. 5, main text).

**Table S1.** Cantilever parameters ( $n$ th eigenmode) in liquid of the figures in the main text and in the Electronic Supplementary Information.

Figure	Type	$n$	$k_n$ [N m <sup>-1</sup> ]	$Q_n$	$f_n$ [kHz]	$\sigma_n$ [nm V <sup>-1</sup> ]
1 a-d	ArrowUHF_AuD	1	8.13	4.8	492	15.8
2 a-d	ArrowUHF_AuD	1	7.45	4.8	463	8.18
3 d-f	ArrowUHF_AuD	1	7.45	4.8	463	8.18
4 a	ArrowUHF_AuD	1	7.03	3.0	547	12.62
5 a-c Top panel	ArrowUHF_AuD	1	7.45	4.8	463	8.18
5 a Middle + bottom panel	ArrowUHF_AuD	1	8.13	4.8	492	15.8
5 b Middle panel	ArrowUHF_AuD	1	9.9	5.6	523	17.57
5 b Bottom panel	PPP-NCH-AuD	2	2150	20	1025	8
5 c Middle panel	PPP-FM-AuD	2	183.7	6	192.1	6.6
5 c Bottom panel	PPP-NCH-AuD	2	1908.62	17.1	910	7.3
S2	FastScan-A <sup>a</sup>	1	15	6	424	10
S3	PPP-NCH-AuD	1	37.7	9.4	142	45.2
S4	ArrowUHF_AuD	1	7.45	4.8	463	8.18
S5	ArrowUHF_AuD	1	7.03	3.0	547	12.62
S6	ArrowUHF_AuD	1	9.63	4.7	525	8.81

<sup>a</sup>Calibrated by using the nominal value for  $k$  (manufacturer specification)

Table S2: Details of the Box Plot shown in Figure 3 (main text). Each value was calculated from between 9 and 46 individual force-distance curves.

			Mean (nm)	Median (nm)	STD <sup>a</sup> (nm)	MAD <sup>b</sup> (nm)
<b>Mica</b>	<b>Fresh</b>	<b><i>d</i><sub>1</sub></b>	0.31	0.31	0.04	0.02
		<b><i>d</i><sub>2</sub></b>	0.34	0.34	0.05	0.04
		<b><i>d</i><sub>3</sub></b>	0.31	0.31	0.02	0.02
	<b>Exposed</b>	<b><i>d</i><sub>1</sub></b>	0.31	0.32	0.04	0.03
		<b><i>d</i><sub>2</sub></b>	0.33	0.33	0.03	0.02
		<b><i>d</i><sub>3</sub></b>	0.34	0.33	0.02	0.02
<b>HOPG</b>	<b>Fresh</b>	<b><i>d</i><sub>1</sub></b>	0.38	0.35	0.12	0.08
		<b><i>d</i><sub>2</sub></b>	0.49	0.47	0.15	0.11
		<b><i>d</i><sub>3</sub></b>	0.47	0.45	0.10	0.06
	<b>Exposed</b>	<b><i>d</i><sub>1</sub></b>	0.45	0.46	0.06	0.05
		<b><i>d</i><sub>2</sub></b>	0.54	0.55	0.05	0.03
		<b><i>d</i><sub>3</sub></b>	0.51	0.51	0.04	0.03

<sup>a</sup> standard deviation, <sup>b</sup> mean average deviation

## SI References

1. D. Martin-Jimenez, E. Chacon, P. Tarazona, R. Garcia, Atomically resolved three-dimensional structures of electrolyte aqueous solutions near a solid surface. *Nat. Commun.* **7**, 12164 (2016).
2. M. R. Uhlig, D. Martin-Jimenez, R. Garcia, Atomic-scale mapping of hydrophobic layers on graphene and few-layer MoS<sub>2</sub> and WSe<sub>2</sub> in water. *Nat. Commun.* **10**, 2606 (2019).
3. D. S. Wastl, A. J. Weymouth, F. J. Giessibl, Atomically resolved graphitic surfaces in air by atomic force microscopy. *ACS Nano* **8**, 5233–5239 (2014).
4. J. E. Sader, J. R. Friend, Note: Calibration of atomic force microscope cantilevers using only their resonant frequency and quality factor. *Rev. Sci. Instrum.* **85**, 116101 (2014).
5. J. E. Sader, J. R. Friend, Note: Improved calibration of atomic force microscope cantilevers using multiple reference cantilevers. *Rev. Sci. Instrum.* **86**, 2014–2016 (2015).
6. A. Labuda, *et al.*, Calibration of higher eigenmodes of cantilevers. *Rev. Sci. Instrum.* **87**, 073705 (2016).
7. J. L. Hutter, J. Bechhoefer, Calibration of atomic-force microscope tips. *Rev. Sci. Instrum.* **64**, 1868–1873 (1993).
8. T. Fukuma, R. Garcia, Atomic- and Molecular-Resolution Mapping of Solid-Liquid Interfaces by 3D Atomic Force Microscopy. *ACS Nano* **12**, 11785–11797 (2018).
9. R. Garcia, *Amplitude Modulation Atomic Force Microscopy* (Wiley-VCH Verlag GmbH & Co. KGaA, 2010) <https://doi.org/10.1002/9783527632183>.
10. E. T. Herruzo, H. Asakawa, T. Fukuma, R. Garcia, Three-dimensional quantitative force maps in liquid with 10 piconewton, angstrom and sub-minute resolutions. *Nanoscale* **5**, 2678–2685 (2013).
11. A. F. Payam, D. Martin-Jimenez, R. Garcia, Force reconstruction from tapping mode force microscopy experiments. *Nanotechnology* **26**, 1–12 (2015).
12. H. Hölscher, Quantitative measurement of tip-sample interactions in amplitude modulation atomic force microscopy. *Appl. Phys. Lett.* **89**, 123109 (2006).
13. A. Temiryazev, A. Frolov, M. Temiryazeva, Atomic-force microscopy study of self-assembled atmospheric contamination on graphene and graphite surfaces. *Carbon N. Y.* **143**, 30–37 (2019).
14. Y.-H. Lu, C.-W. Yang, C.-K. Fang, H.-C. Ko, I.-S. Hwang, Interface-Induced Ordering of Gas Molecules Confined in a Small Space. *Sci. Rep.* **4**, 7189 (2015).
15. P. Gallagher, *et al.*, Switchable friction enabled by nanoscale self-assembly on graphene. *Nat. Commun.* **7**, 1–7 (2016).
16. P. Gallagher, *et al.*, Optical Imaging and Spectroscopic Characterization of Self-Assembled Environmental Adsorbates on Graphene. *Nano Lett.* **18**, 2603–2608 (2018).
17. D. S. Wastl, *et al.*, Observation of 4 nm pitch stripe domains formed by exposing graphene to ambient air. *ACS Nano* **7**, 10032–10037 (2013).
18. I. Schlesinger, U. Sivan, Three-Dimensional Characterization of Layers of Condensed Gas Molecules Forming Universally on Hydrophobic Surfaces. *J. Am. Chem. Soc.* **140**, 10473–10481 (2018).
19. W. Foster, J. A. Aguilar, H. Kusumaatmaja, K. Voitchovsky, In Situ Molecular-Level Observation of Methanol Catalysis at the Water–Graphite Interface. *ACS Appl. Mater. Interfaces* **10**, 34265–34271 (2018).
20. Y. Zou, A. S. Walton, I. A. Kinloch, R. A. W. Dryfe, Investigation of the Differential Capacitance of Highly Ordered Pyrolytic Graphite as a Model Material of Graphene. *Langmuir* **32**, 11448–11455 (2016).
21. N. Nioradze, *et al.*, Organic contamination of highly oriented pyrolytic graphite as studied by scanning electrochemical microscopy. *Anal. Chem.* **87**, 4836–4843 (2015).
22. J. M. Hurst, L. Li, H. Liu, Adventitious hydrocarbons and the graphite-water interface. *Carbon N. Y.* **134**, 464–469 (2018).
23. E. R. Azhagiya Singam, *et al.*, Thermodynamics of Adsorption on Graphenic Surfaces from Aqueous Solution. *J. Chem. Theory Comput.* **15**, 1302–1316 (2019).
24. J. Comer, R. Chen, H. Poblete, A. Vergara-Jaque, J. E. Riviere, Predicting Adsorption Affinities of Small Molecules on Carbon Nanotubes Using Molecular Dynamics Simulation.

- ACS Nano **9**, 11761–11774 (2015).
25. J. C. Phillips, *et al.*, Scalable molecular dynamics with NAMD. *J. Comput. Chem.* **26**, 1781–1802 (2005).
  26. S. E. Feller, Y. Zhang, R. W. Pastor, B. R. Brooks, Constant pressure molecular dynamics simulation: The Langevin piston method. *J. Chem. Phys.* **103**, 4613–4621 (1995).
  27. C. W. Hopkins, S. Le Grand, R. C. Walker, A. E. Roitberg, Long-Time-Step Molecular Dynamics through Hydrogen Mass Repartitioning. *J. Chem. Theory Comput.* **11**, 1864–1874 (2015).
  28. D. M. York, T. A. Darden, L. G. Pedersen, The effect of long-range electrostatic interactions in simulations of macromolecular crystals: A comparison of the Ewald and truncated list methods. *J. Chem. Phys.* **99**, 8345–8348 (1993).
  29. W. L. Jorgensen, J. Chandrasekhar, J. D. Madura, R. W. Impey, M. L. Klein, Comparison of simple potential functions for simulating liquid water. *J. Chem. Phys.* **79**, 926–935 (1983).
  30. S. Miyamoto, P. A. Kollman, Settle: An analytical version of the SHAKE and RATTLE algorithm for rigid water models. *J. Comput. Chem.* **13**, 952–962 (1992).
  31. H. C. Andersen, Rattle: A “velocity” version of the shake algorithm for molecular dynamics calculations. *J. Comput. Phys.* **52**, 24–34 (1983).
  32. K. Vanommeslaeghe, *et al.*, CHARMM general force field: A force field for drug-like molecules compatible with the CHARMM all-atom additive biological force fields. *J. Comput. Chem.* **31** (2010).
  33. J. Calbo, *et al.*, Understanding Noncovalent Interactions of Small Molecules with Carbon Nanotubes. *Chem. - A Eur. J.* **23**, 12909–12916 (2017).
  34. R. T. Cygan, J.-J. Liang, A. G. Kalinichev, Molecular Models of Hydroxide, Oxyhydroxide, and Clay Phases and the Development of a General Force Field. *J. Phys. Chem. B* **108**, 1255–1266 (2004).
  35. J. Wang, A. G. Kalinichev, R. J. Kirkpatrick, R. T. Cygan, Structure, Energetics, and Dynamics of Water Adsorbed on the Muscovite (001) Surface: A Molecular Dynamics Simulation. *J. Phys. Chem. B* **109**, 15893–15905 (2005).
  36. A. A. Skelton, P. Fenter, J. D. Kubicki, D. J. Wesolowski, P. T. Cummings, Simulations of the Quartz(10 $\bar{1}$ 1)/Water Interface: A Comparison of Classical Force Fields, Ab Initio Molecular Dynamics, and X-ray Reflectivity Experiments. *J. Phys. Chem. C* **115**, 2076–2088 (2011).
  37. D. R. Heine, A. R. Rammohan, J. Balakrishnan, Atomistic simulations of the interaction between lipid bilayers and substrates. *Mol. Simul.* **33**, 391–397 (2007).
  38. S. Kang, *et al.*, Hydrophobic Interaction Drives Surface-Assisted Epitaxial Assembly of Amyloid-like Peptides. *J. Am. Chem. Soc.* **135**, 3150–3157 (2013).
  39. M. Ricci, P. Spijker, K. Voïtchovsky, Water-induced correlation between single ions imaged at the solid-liquid interface. *Nat. Commun.* **5**, 4400 (2014).
  40. B. R. Brooks, *et al.*, CHARMM: A program for macromolecular energy, minimization, and dynamics calculations. *J. Comput. Chem.* **4**, 187–217 (1983).
  41. K. Vanommeslaeghe, A. D. MacKerell, Automation of the CHARMM General Force Field (CGenFF) I: Bond Perception and Atom Typing. *J. Chem. Inf. Model.* **52**, 3144–3154 (2012).
  42. K. Vanommeslaeghe, E. P. Raman, A. D. MacKerell, Automation of the CHARMM General Force Field (CGenFF) II: Assignment of Bonded Parameters and Partial Atomic Charges. *J. Chem. Inf. Model.* **52**, 3155–3168 (2012).
  43. H. Poblete, I. Miranda-Carvajal, J. Comer, Determinants of Alanine Dipeptide Conformational Equilibria on Graphene and Hydroxylated Derivatives. *J. Phys. Chem. B* **121**, 3895–3907 (2017).
  44. W. Humphrey, A. Dalke, K. Schulten, VMD: Visual molecular dynamics. *J. Mol. Graph.* **14**, 33–38 (1996).
  45. M. D. Hanwell, *et al.*, Avogadro: an advanced semantic chemical editor, visualization, and analysis platform. *J. Cheminform.* **4**, 17 (2012).
  46. A. Kohlmeyer, J. Vermaas, No Title (2017) <https://doi.org/10.5281/zenodo.545655>.
  47. P. E. M. Lopes, V. Murashov, M. Tazi, E. Demchuk, A. D. MacKerell, Development of an

- Empirical Force Field for Silica. Application to the Quartz–Water Interface. *J. Phys. Chem. B* **110**, 2782–2792 (2006).
48. E. Darve, A. Pohorille, Calculating free energies using average force. *J. Chem. Phys.* **115**, 9169–9183 (2001).
  49. J. Comer, *et al.*, The Adaptive Biasing Force Method: Everything You Always Wanted To Know but Were Afraid To Ask. *J. Phys. Chem. B* **119**, 1129–1151 (2015).
  50. G. Fiorin, M. L. Klein, J. Hénin, Using collective variables to drive molecular dynamics simulations. *Mol. Phys.* **111**, 3345–3362 (2013).
  51. C. Chipot, J. Comer, Subdiffusion in Membrane Permeation of Small Molecules. *Sci. Rep.* **6**, 35913 (2016).
  52. G. Hummer, Position-dependent diffusion coefficients and free energies from Bayesian analysis of equilibrium and replica molecular dynamics simulations. *New J. Phys.* **7**, 34–34 (2005).
  53. J. Comer, C. Chipot, F. D. González-Nilo, Calculating Position-Dependent Diffusivity in Biased Molecular Dynamics Simulations. *J. Chem. Theory Comput.* **9**, 876–882 (2013).
  54. R. B. Best, G. Hummer, Diffusion models of protein folding. *Phys. Chem. Chem. Phys.* **13**, 16902 (2011).